




Article

In Situ Preparation of Three-Dimensional Porous Nickel Sulfide as a Battery-Type Supercapacitor

Qixun Xia ^{1,†} , Lijun Si ^{1,†}, Keke Liu ¹, Aiguo Zhou ¹ , Chen Su ¹, Nanasaheb M. Shinde ^{2,*} , Guangxin Fan ¹ and Jun Dou ^{3,*}

¹ School of Materials Science and Engineering, Henan Polytechnic University, Jiaozuo 454003, China; 212006010012@home.hpu.edu.cn (L.S.)

² Department of Chemical Engineering (BK21 FOUR), Dong-A University, 37 Nakdong-daero, Saha-gu, Busan 49315, Republic of Korea

³ Postdoctoral Workstation in LB Group Co., Ltd., Jiaozuo 454000, China

* Correspondence: nanashinde2009@gmail.com (N.M.S.); doujun@lomonbillions.com (J.D.)

† These authors contribution equally to this work.

Abstract: A one-step sulfurization method to fabricate Ni₃S₂ nanowires (Ni₃S₂ NWs) directly on a Ni foam (NF) was developed as a simple, low-cost synthesis method for use as a supercapacitor (SC), aimed at optimizing energy storage. Ni₃S₂ NWs have high specific capacity and are considered a promising electrode material for SCs; however, their poor electrical conductivity and low chemical stability limit their applications. In this study, highly hierarchical three-dimensional porous Ni₃S₂ NWs were grown directly on NF by a hydrothermal method. The feasibility of the use of Ni₃S₂/NF as a binder-free electrode for achieving high-performance SCs was examined. Ni₃S₂/NF exhibited a high specific capacity (255.3 mAh g⁻¹ at a current density of 3 A g⁻¹), good rate capability (2.9 times higher than that of the NiO/NF electrode), and competitive cycling performance (capacity retention of specific capacity of 72.17% after 5000 cycles at current density of 20 A g⁻¹). Owing to its simple synthesis process and excellent performance as an electrode material for SCs, the developed multipurpose Ni₃S₂ NWs electrode is expected to be a promising electrode for SC applications. Furthermore, the synthesis method of self-growing Ni₃S₂ NW electrodes on 3D NF via hydrothermal reactions could potentially be applied to the fabrication of SC electrodes using a variety of other transition metal compounds.

Keywords: nickel sulfide; supercapacitor; crystal growth; porous materials



Citation: Xia, Q.; Si, L.; Liu, K.; Zhou, A.; Su, C.; Shinde, N.M.; Fan, G.; Dou, J. In Situ Preparation of Three-Dimensional Porous Nickel Sulfide as a Battery-Type Supercapacitor. *Molecules* **2023**, *28*, 4307. <https://doi.org/10.3390/molecules28114307>

Academic Editors: Hassan Hasan Hammud and Nadeem S. Sheikh

Received: 15 March 2023

Revised: 18 May 2023

Accepted: 22 May 2023

Published: 24 May 2023



Copyright: © 2023 by the authors. Licensee MDPI, Basel, Switzerland. This article is an open access article distributed under the terms and conditions of the Creative Commons Attribution (CC BY) license (<https://creativecommons.org/licenses/by/4.0/>).

1. Introduction

Supercapacitors (SCs) have garnered considerable attention in the field of next-generation electronics, which include various portable electronic devices, autonomous electric vehicles, and roll-up displays. This may be attributed to their excellent performance in terms of power density, charge/discharge rates and cycling stability. SCs possess higher energy density, a faster charging/discharging rate (within a few seconds), much greater power density, and a longer cycle life than rechargeable batteries [1–5]. Transitional metal oxides, such as RuO₂ [6], NiO [7], MnO₂ [8], and their mixed oxides, have emerged as potential candidates for SC electrode materials [9–12]. This can be attributed to their small band gap and abundant active sites, which result in better electronic conductivity and higher theoretical capacity than that of mono-metal oxides [13]. Among the transition metal oxides, nickel-based oxides are widely used to prepare SC electrodes, owing to their high theoretical specific capacitance [14–18], abundance, and easy preparation methods. Further, compared to metal oxides, metal sulfides exhibit superior electrical conductivity and higher electrochemical activity. Although certain metal sulfides do not have a band gap or electronic structure, they exhibit typical metallic behaviors, which in turn lead to fast redox reaction kinetics [19]. However, the low electron conductivity and non-robust nanostructure of NiO (80.09% capacitance retention after 10,000 cycles) lead to

poor rate capability and cycling stability [20]. The electrical conductivity of NiS is at least two orders of magnitude higher than that of NiO and, hence, the former provides outstanding electrochemical activity [20]. Moreover, the performance of electrochemical devices is known to be drastically influenced by their architectures. Among micro/nanomaterials for SCs, materials with one-dimensional (1D) or two-dimensional (2D) architectures with high aspect ratios, low densities, and high surface areas have garnered considerable attention. Cai et al. [21] reported a honeycomb-like nickel–manganese sulfide (NMS) composite nanosheet with a high specific capacity of 205 mAh g⁻¹ (at 2 mA cm⁻²). Wei et al. [22] synthesized α -NiS hollow-sphere electrodes with a specific capacitance of 562.3 F g⁻¹ (at 0.6 A g⁻¹). Wang et al. [23] developed a two-step strategy to synthesize an Ni_xS_y (Ni₃S₄ and NiS₂)/MoS₂ hybrid nanomaterial for use as a high-performance electrode. The loose structure of this hybrid nanomaterial favors ion diffusion. When utilized as an electrode, the as-synthesized electrode exhibited a high specific capacity (169.44 mAh g⁻¹ at 1 A g⁻¹), excellent cycling stability (\approx 88.24% capacity retention after 8000 charge/discharge tests), and excellent rate performance (rate performance of 64.9% for 1–20 A g⁻¹). Wang et al. [24] synthesized rigid three-dimensional (3D) Ni₃S₄ nanosheet frames assembled from ultrathin NW via a facile solvothermal method. Compared to flat Ni₃S₄ sheets, the 3D Ni₃S₄ nanosheet frames possess a larger free volume and higher compressive strength, in addition to being able to deliver an exceptional specific capacitance of 1213 F g⁻¹. The electrochemical storage principle of energy storage materials—closely related to the types of ions present in the electrolytes. Mu et al. [25] combined density functional theory (DFT) calculations and an in situ X-ray diffraction (XRD) technique to investigate the charge-storage mechanism of MXene in H₂SO₄ and confirmed that the c-lattice of Ti₃C₂ changes with H⁺ intercalation because of the steric effect in conjunction with the action of the electrostatic force. By combining first-principle calculations and the implicit solvation model and investigating the electronic states during the charge process, Ando et al. [26] proposed the interaction between partially intercalated dehydrated cations and MXene layers. Chen et al. [27] deduced that the charge-storage mechanism of V₂C may be closely related to the size of cations; cations with smaller radii, such as Mg²⁺ and Li⁺, were intercalated into the interlayer space, and they interacted with the surface V atoms and termination groups. In contrast, larger ions such as Na⁺ and K⁺ could only access a few shallow sites, thereby contributing to superior rate and cycling performance. Hence, 1 M KOH solution was selected as the electrolyte in this work.

However, challenges still remain in the practical application of nickel sulfide; novel structures are necessary to improve the energy storage efficiency [28]. Metal sulfides commonly exhibit superior electrical conductivity and higher electrochemical activity compared to metal oxides. Among metal sulfides, nickel-based sulfides are regarded as particularly attractive because of their enhanced conductivity, abundant redox sites, high structural robustness, and mechanical strength.

In order to achieve the aforementioned objective, we fabricated Ni₃S₂ NW supported on Ni foam (NF) via a one-step sulfurization process. The Ni₃S₂ NW was directly formed on the conducting NF, which possesses a large active surface area responsible for rapid electrolyte-ion transportation. Our experimental results demonstrated that Ni₃S₂ NW exhibits excellent conductivity and a yielding structure, which play key roles in high-performance electrode materials. To develop high-performance asymmetric SC (ASC) devices, we deposited and fabricated Ni₃S₂ NW and MXene nanostructures that can be used as electrodes without any conductive additives or binders. Notably, the 3D NF substrates provide a unique structure for the SC electrode, which makes it suitable for applications in energy devices. This advantage motivated us to fabricate a 3D Ni₃S₂/NF electrode with a well-arranged nanostructure. The developed Ni₃S₂ NW can serve as a SC electrode with excellent stability.

2. Results and Discussion

An overview of the fabrication strategy of hierarchical Ni₃S₂ NW on a 3D NF surface to construct a binder-free self-supported nanoarray is provided in Figure 1. This method

first outlines the synthesis of Ni(OH)₂/NF via a hydrothermal method. Next, Na₂S acts as the sulfur source and S²⁻ ions are released during the hydrolysis of Na₂S. Ni²⁺ and S²⁻ ions can easily combine to precipitate Ni₃S₂ under hydrothermal conditions [29]. Finally, Ni(OH)₂ and Na₂S react to form the Ni₃S₂ NW via the following reactions:

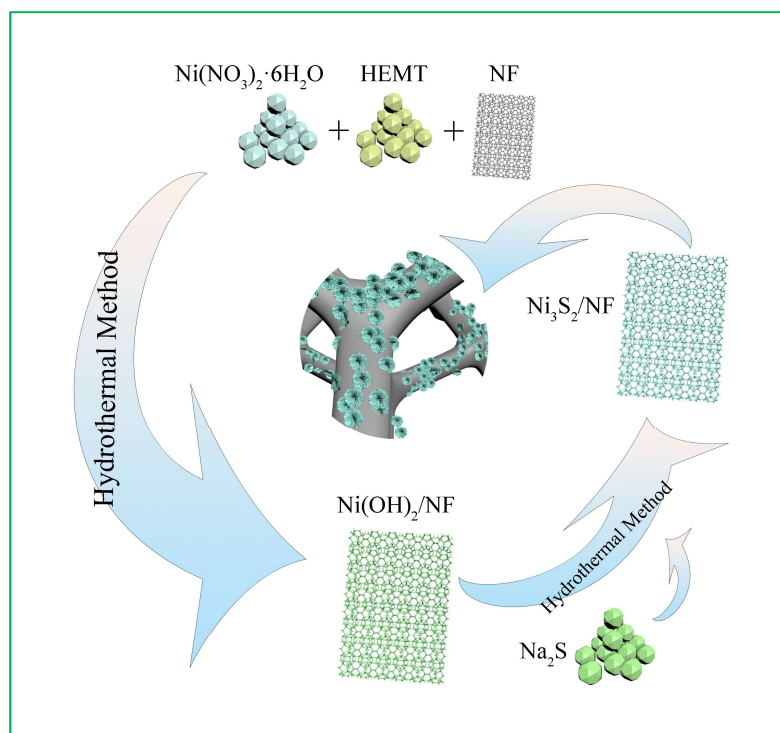


Figure 1. Schematic diagram of the fabrication methodology for the Ni₃S₂/NF hybrid.

The nanosized Ni₃S₂/NF material was grown vertically in situ on NF. The NF exhibits a typical morphology of a 3D cross-linked porous framework that facilitates ion transport in electrochemical reactions. Its unique structure contains several voids and provides ample active sites for electrochemical reactions [30]. Furthermore, this 3D porous honeycomb-like structure helps avoid the congestion of electrolyte ions and provides a large exposed surface area, ensuring efficient ion diffusion and a sufficient Faradaic redox reaction [14].

Figure 2 shows the phase compositions and crystal structures of NF, NiO, and Ni₃S₂ based on XRD analyses. The peaks located at 37.27°, 43.35°, and 63.16° were identified as the (111), (200), and (220) planes of NiO (JCPDS 78-0643), respectively. The diffraction peaks at 21.70°, 31.09°, 49.71°, 50.23°, and 55.35° aligned well with the (101), (110), (113), (211), and (122) planes of Ni₃S₂ (JCPDS 00-030-0863), respectively. The diffraction peaks located at 44.65°, 52.02°, and 76.51° for NiF (JCPDS 04-0850) were assigned to (111), (200), and (220) crystal planes, respectively. The XRD pattern clearly revealed that all the NiF and NiO/NF were successfully transformed into the hybrid Ni₃S₂/NF material.

The SEM morphologies of the NiO/NF and Ni₃S₂/NF electrodes are shown in Figure 3. After sulfidation, Ni₃S₂ NW were uniformly dispersed on the NF and were tightly anchored to the NF networks (Figure 3a,c). Both Figure 3b,d show 3D NW structures. Compared with NiO/NF, Ni₃S₂/NF had more tightly bonded NWs and NF; this special structure enables it to withstand more stringent redox reactions in alkaline electrolyte, resulting in enhanced cycling stability.

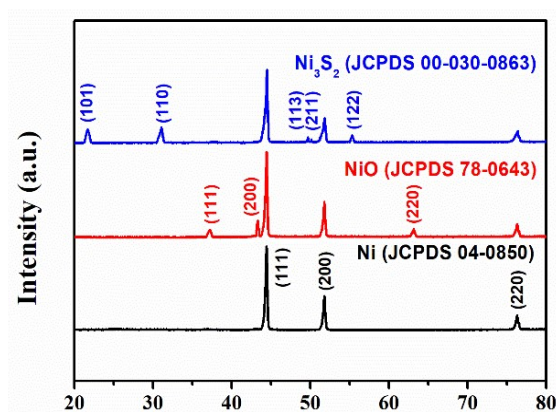


Figure 2. X-ray diffraction (XRD) patterns of nickel foam (NF), NiO/NF, and Ni₃S₂/NF.

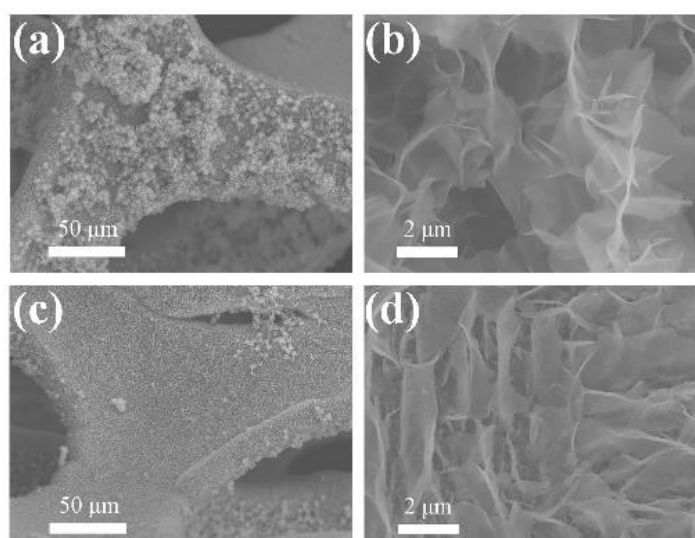


Figure 3. Scanning electron microscopy (SEM) images of (a,b) NiO/NF and (c,d) Ni₃S₂/NF.

For further insight into the morphology and microstructure of the as-fabricated Ni₃S₂ materials, we performed high-resolution transmission electron microscopy (HRTEM).

As shown in Figure 4a, the low-magnification TEM image confirmed the NWs-like structure of Ni₃S₂. The HRTEM images shown in Figure 4b present a clear lattice of 0.28 nm, which matched well with the (110) plane of Ni₃S₂. The selected-area electron diffraction (SEAD) pattern (Figure 4c) shows several concentric rings, indicating the polycrystalline structure of Ni₃S₂ NW [31]. Figure 4d clearly illustrates the uniform distribution of Ni and S elements in the hybrid material.

The surface area, pore types, and pore-size distributions of NiO and Ni₃S₂ were investigated based on nitrogen adsorption/desorption isotherms and the BJH pore-size distribution, as shown in Figure 5. The N₂ adsorption/desorption isotherms of NiO and Ni₃S₂ indicate slit-like pores in the Ni₃S₂ mesoporous structure, as shown in Figure 5a,c. The specific BET surface areas of NiO and Ni₃S₂ were 2.2 and 32.3 m² g^{−1}, respectively, and their average pore sizes were 18 and 37.1 nm, respectively. Figure 3b,d show the BJH (the Barret, Joyner, and Halenda method) pore-size distributions of NiO and Ni₃S₂; the three main peaks at 2.7, 6.5, and 45.3 nm for NiO and the local peak at 40.0 nm for Ni₃S₂ indicate excess mesoscale pores in both NiO and Ni₃S₂. Ashkan et al. [32] studied the Li intercalation/deintercalation in bulk LiCoO₂ and at the LiCoO₂ (10 $\bar{1}$ 4) surface using DFT calculations and found that the diffusion barriers between the topmost second and third layers are lower than those in bulk LiCoO₂. This finding indicated that nanosized LiCoO₂ with a large surface area/volume ratio is a promising cathode material for fast charging/discharging Li-ion batteries. Wang et al. [33] also suggested

that both the electrochemically active surface area and the internal structure contribute to the effective diffusion coefficient. Pseudocapacitors store electric charges via rapid and surface/near-surface controlled non-diffusion limited Faradaic redox reactions. According to Equation (3), a large ion-accessible surface area can generate high capacitance in a certain electrolyte [34].

$$C = \frac{\epsilon_r \epsilon_0}{d} A, \quad (3)$$

where ϵ_r , ϵ_0 , d , and A represent the permittivity of the vacuum ($\text{F}\cdot\text{m}^{-1}$), the relative dielectric constant of the electrolyte solution, the distance between the electrolyte ions, and the electrode surface (m) and ion-accessible surface area of the electrode material (m^2), respectively. Considering the results of XRD, SEM, HR-TEM, and BET characterization analyses of NiO and Ni_3S_2 electrodes and the simple synthesis process, we believe that the attractive nanostructure can be employed for energy-storage applications. The three electrode-based electrochemical measurements of the Ni_3S_2 and NiO electrodes were evaluated using cyclic voltammetry, GCD, and electrochemical impedance spectroscopy (EIS) results obtained for a 1 M KOH aqueous electrolyte solution. Figure 6a,b show a pair of redox peaks in each CV curve, revealing that the typical pseudocapacitance of Ni_3S_2 and NiO electrode materials can be attributed to the redox mechanism, and the possible chemical reactions can be described as follows [31,35,36]:

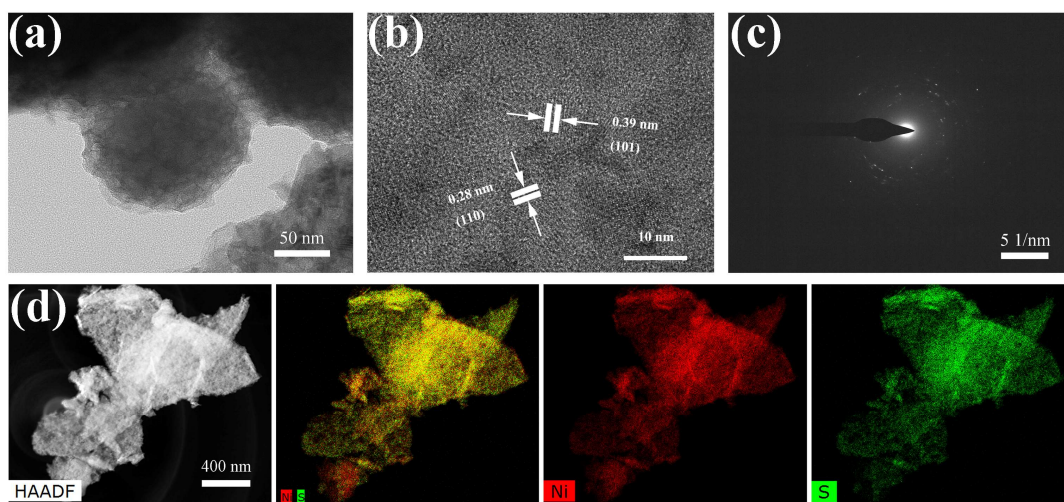
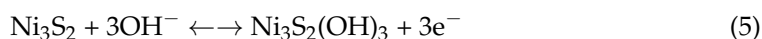
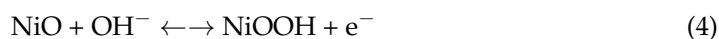


Figure 4. (a) Transmission electron microscopy (TEM), (b) high-resolution TEM (HRTEM), (c) selected-area electron diffraction (SEAD) pattern, (d) energy dispersive X-ray spectroscopy (EDS)–high-angle annular dark field images and the corresponding elemental mapping of Ni_3S_2 .

The peak current increases with the scanning rate, indicating that the electrode has high-rate capability [37]. Notably, the peak current value of Ni_3S_2 is higher than that of NiO because Ni_3S_2 has a dense lamellar structure (as shown in the SEM images in Figure 2), which is conducive to rapid electrolyte–ion transport. Figure 6c,d show the GCD curves of NiO/NF and Ni_3S_2 /NF at different current densities ($3\text{--}20 \text{ A g}^{-1}$). The GCD curves of both materials exhibit Faraday capacitance characteristics; this finding agrees well with the CV results. Furthermore, the charge/discharge time increased from 332.2 s for NiO/NF to 639.2 s for Ni_3S_2 /NF at 3 A g^{-1} , indicating that the latter had a higher specific capacity. The specific capacity of the Ni_3S_2 /NF electrode (255.3 mAh g^{-1}) was much higher than that of the NiO electrode (138 mAh g^{-1}) at a current density of 3 A g^{-1} ; even at a high current density of 20 A g^{-1} , the Ni_3S_2 /NF hybrid electrode still possessed

a high specific capacity of 111.1 mAh g^{-1} (the specific capacity of the NiO/NF electrode was 26.7 mAh g^{-1}), indicating the superior electrochemical performance of the $\text{Ni}_3\text{S}_2/\text{NF}$ electrode (Figure 7d). During oxidation, the chemical state of S^{2-} does not change, but valence transitions from Ni^0 to Ni^+ and further to Ni^{3+} occur sequentially. Hence, we inferred that the reversible Faradaic reactions of Ni_3S_2 in KOH aqueous solution can be attributed to the valence transitions of Ni^0 in Ni_3S_2 between Ni^0 and Ni^{3+} . Therefore, according to the results deduced from both CV curves and XPS spectra, the two-step oxidation process and the three-step reverse-reduction process in the reversible Faradaic reaction proceed as shown in Equations (6) and (7), respectively [35]:

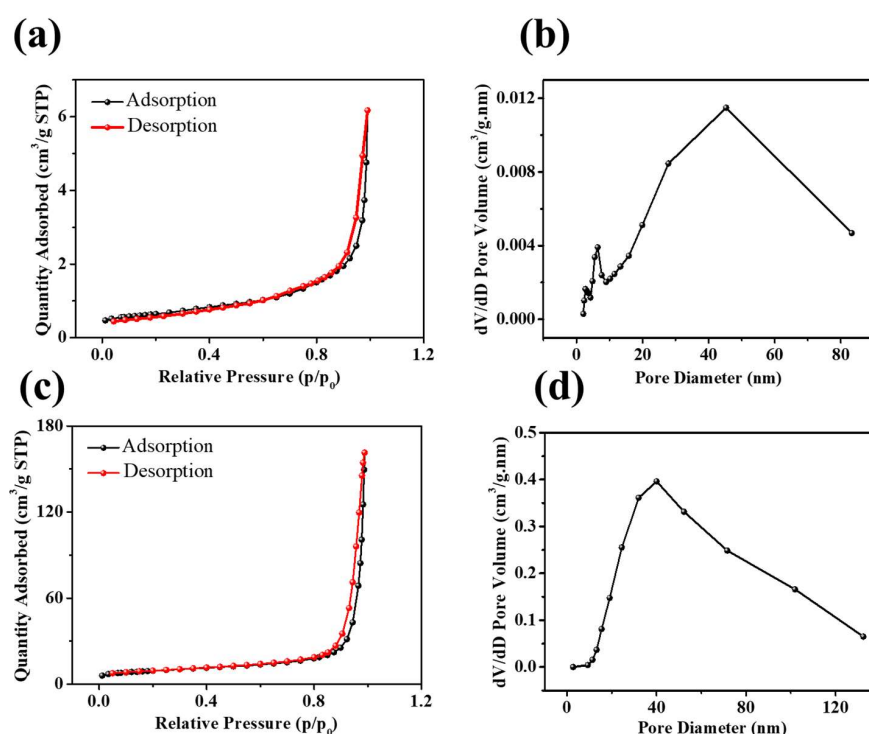
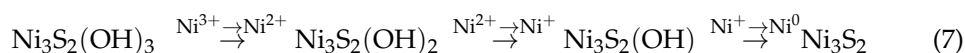
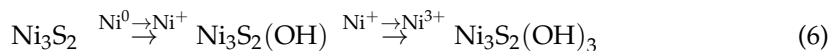


Figure 5. N_2 adsorption/desorption isotherms of (a) NiO and (c) Ni_3S_2 ; the pore-size distributions of (b) NiO and (d) Ni_3S_2 .

As illustrated in Figure 7a, the CV curve of NF exhibits an approximately linear shape, indicating that the contribution of the NF in the hybrid to the capacity of the material is negligible. Moreover, the CV curve of the $\text{Ni}_3\text{S}_2/\text{NF}$ electrode has a considerably more enhanced integral area than that of the NiO/NF electrode, implying that the $\text{Ni}_3\text{S}_2/\text{NF}$ electrode has superior specific capacity; this finding is consistent with the GCD curve comparison (Figure 7c). The plots of the current density against the square root of the scan rate for NiO/NF and $\text{Ni}_3\text{S}_2/\text{NF}$ are shown in Figure 7b. i_p increased linearly with $\nu^{1/2}$, confirming that the Faradic capacities of both electrodes were limited by the electrolyte-ion permeation to the active sites. The Randles–Sevcik equation [38,39] was used to compute the diffusion coefficient of the NiO/NF and $\text{Ni}_3\text{S}_2/\text{NF}$ electrodes:

$$i_p = (2.69 \times 10^5) n^{3/2} A D_0^{1/2} C_0^* \nu^{1/2}, \quad (8)$$

where i_p , n , A , D_0 , C_0^* , and ν are the peak current, the number of electrons transferred, the electrode area, the diffusion coefficient, the reactant concentration, and the scan rate, respectively. The diffusion coefficients ($D_{\text{NiO/NF}}$ and $D_{\text{Ni}_3\text{S}_2/\text{NF}}$) of the NiO/NF and $\text{Ni}_3\text{S}_2/\text{NF}$

electrodes were calculated using Equation (9), assuming the same n , A , and C_0^* values for both electrodes. The $\text{Ni}_3\text{S}_2/\text{NF}$ electrode ($D_{\text{Ni}_3\text{S}_2/\text{NF}}$) was 2.9 times that of the NiO/NF electrode. This difference is attributed to the compact Ni_3S_2 nanostructure, which is conducive to the rapid diffusion of electrolyte ions.

$$\frac{D_{\text{Ni}_3\text{S}_2/\text{NF}}}{D_{\text{NiO}}} = \left[\frac{\left(\frac{i_p}{v^{1/2}}\right)_{\text{Ni}_3\text{S}_2/\text{NF}}}{\left(\frac{i_p}{v^{1/2}}\right)_{\text{NiO}}} \right]^2 = \left(\frac{28.46207}{16.62118} \right)^2 = 2.932 \quad (9)$$

The fitted line of the $\text{Ni}_3\text{S}_2/\text{NF}$ electrode has a higher slope than that of the NiO/NF electrode, indicating faster ion diffusion kinetics of the $\text{Ni}_3\text{S}_2/\text{NF}$ electrode. The outstanding electrochemical performance of the NiO/NF and $\text{Ni}_3\text{S}_2/\text{NF}$ samples were further analyzed based on the EIS results shown in Figure 7e. The Nyquist impedance plot (Figure 7e) comprises two parts: a large linear portion in the low frequency range and a semicircular part at high frequencies. In the figure, R_s is the equivalent series resistance, which comprises the electrolyte resistance, intrinsic resistance of the active materials, and contact resistance at the interface between the current collector and the active materials. C_{dl} is the double-layer capacitance, R_{ct} is the charge transfer resistance, and Z_W is the Warburg impedance. Figure 7e shows the Nyquist plots of NiO/NF and $\text{Ni}_3\text{S}_2/\text{NF}$. R_{ct} is low in the high frequency region and has a larger slope in the low frequency region for the $\text{Ni}_3\text{S}_2/\text{NF}$ electrode, indicating lower charge transfer resistance, lower diffusion resistance, and faster ion transport in the electrolyte in the case of the $\text{Ni}_3\text{S}_2/\text{NF}$ electrode [40]. As shown in Figure 7f, the $\text{Ni}_3\text{S}_2/\text{NF}$ electrode still retained a specific capacity of 72.17% after 5000 cycles (at a current density of 20 A g^{-1}), indicating good cycling stability; this value exceeded that of the NiO/NF electrode (62.38%). The enhanced cycling stability of the $\text{Ni}_3\text{S}_2/\text{NF}$ electrode can be attributed to its unique structure, abundant active sites, low resistance, and the synergistic effects of components.

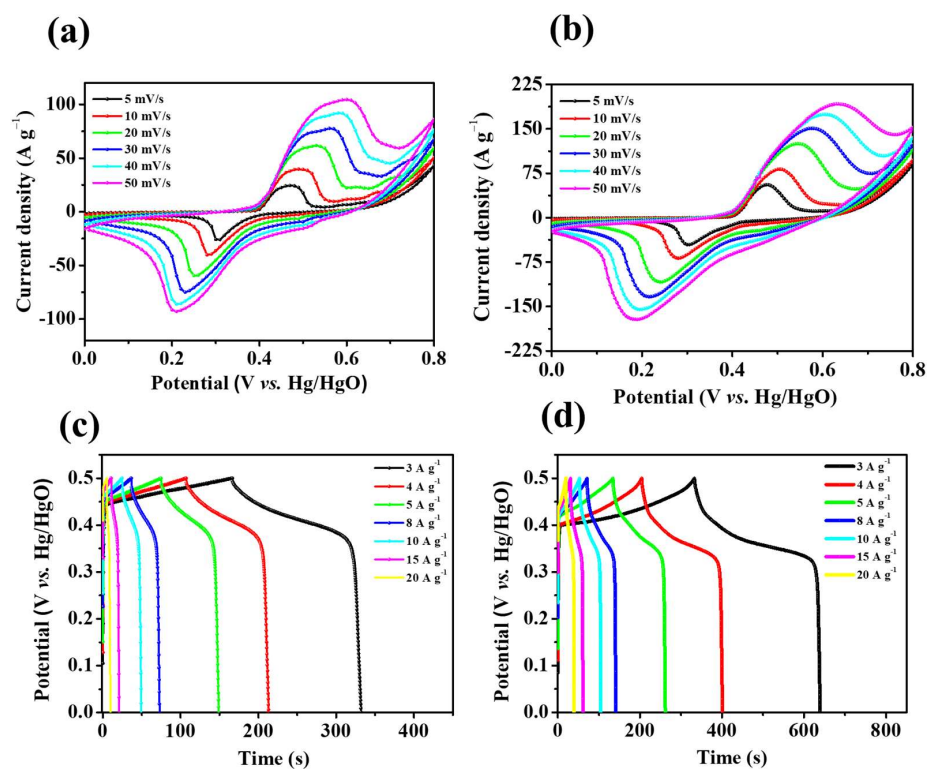


Figure 6. Cyclic voltammogram (CV) curves of (a) NiO/NF and (b) $\text{Ni}_3\text{S}_2/\text{NF}$, (c) GCD curves of NiO/NF and (d) $\text{Ni}_3\text{S}_2/\text{NF}$.

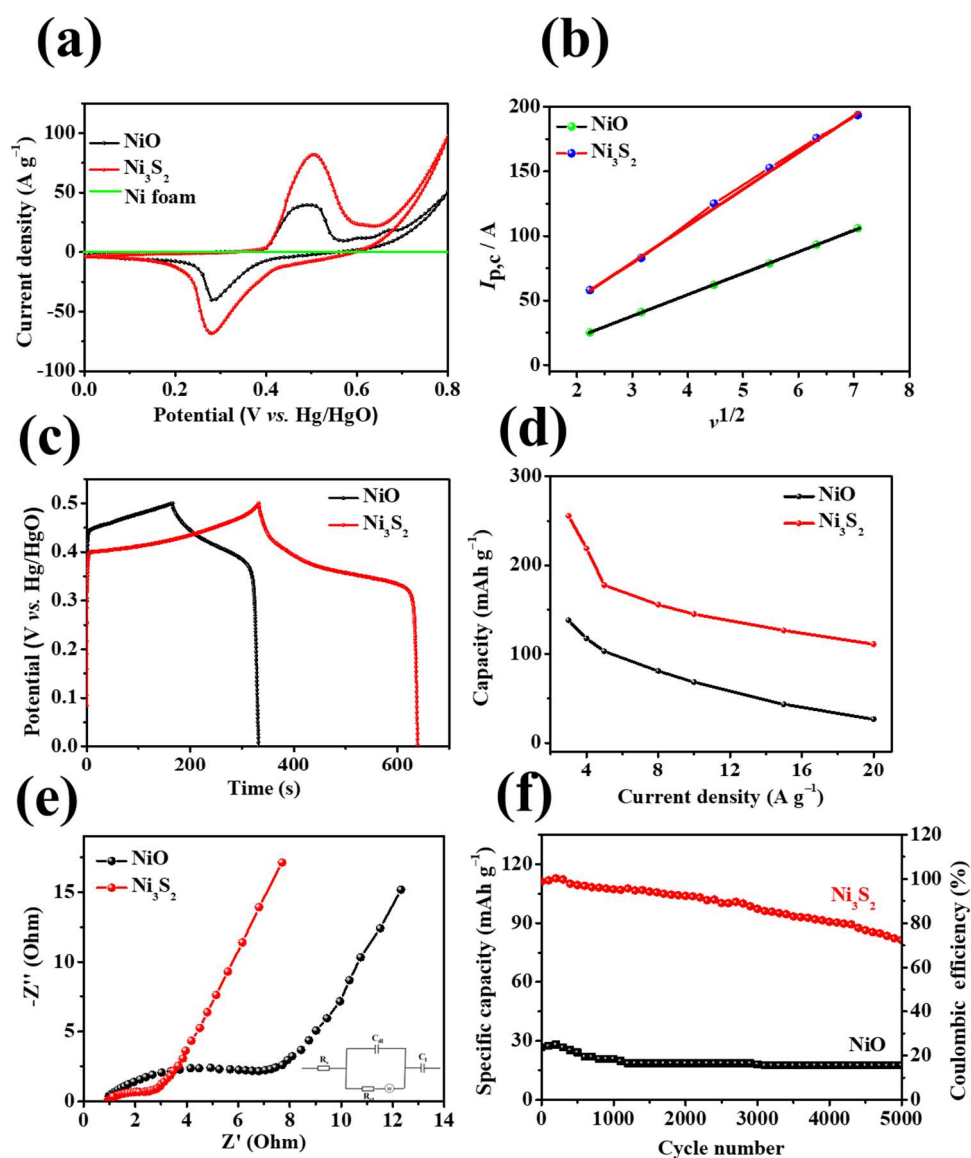


Figure 7. (a) CV curves and of NF, NiO/NF, and Ni₃S₂/NF at 10 mV s⁻¹; (b) plot of the current density to the square root of the scan rate, (c) GCD curves at 3 A g⁻¹, (d) specific capacity at various current densities, (e) EIS and (f) cycling performances of the NiO/NF and Ni₃S₂/NF electrodes.

Cycling stability is a crucial parameter for evaluating the electrochemical performance of Ni₃S₂/NF electrode material. Figure 8a–d show the SEM images of the NiO/NF electrodes and Ni₃S₂/NF electrodes after 5000 cycles. The gradual increase in capacitance during the cycles may be attributed to the activation of the Ni₃S₂/NF electrode materials through the slow intercalation of the electrolyte into the gaps between the nanowires of Ni₃S₂/NF. The low-magnification SEM images in Figure 8a,c indicate that the NiO/NF and Ni₃S₂/NF sample can be seen to be different from the previous morphology (Figure 3a,c). The NWs structure of the NiO/NF disappeared completely after 5000 cycles (Figure 8b). The Ni₃S₂/NF still maintained its NWs structure after 5000 cycles, exhibiting good cycling stability (Figure 8d). The electrochemical performance of the Ti₃C₂T_x material was previously reported [41]. Hence, such unexpected cycling stability of the Ni₃S₂/NF sample can be attributed to the excellent morphological, structural, and compositional stabilities of the Ni₃S₂/NF sample. All the aforementioned findings reveal that the Ni₃S₂/NF sample may be a practical candidate for applications in high-performance electrodes for energy storage. This supposition was further established via comparisons with other NiO/NF electrodes and pristine electrode materials. The large surface areas of self-grown Ni₃S₂/NF samples

are responsible for the enhanced contact between the electrolytes and the $\text{Ni}_3\text{S}_2/\text{NF}$ sample. In the $\text{Ni}_3\text{S}_2/\text{NF}$ sample, nanowires were self-grown directly on the NF via a hydrothermal method. The Ni_3S_2 NWs adhered strongly to the NF. These Ni_3S_2 NWs can be used directly as an SC electrode without any binders or conducting agents. Therefore, the hydrothermal route described herein is an environment-friendly approach that is strongly recommended for fabricating other self-supported electrodes.

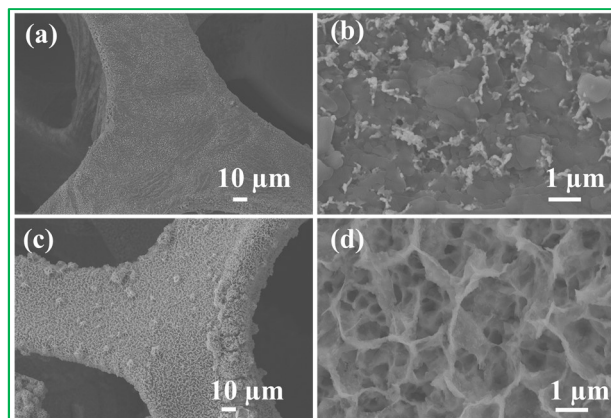


Figure 8. SEM images of (a,b) NiO/NF and (c,d) $\text{Ni}_3\text{S}_2/\text{NF}$ after 5000 cycles numbers.

To explore the application of $\text{Ni}_3\text{S}_2/\text{NF}$ in energy storage applications, we fabricated a $\text{Ti}_3\text{C}_2\text{T}_x$ -based asymmetric coin cell device. In this device, $\text{Ni}_3\text{S}_2/\text{NF}$ and $\text{Ti}_3\text{C}_2\text{T}_x$ served as the positive and negative electrodes, respectively. The electrochemical properties of the $\text{Ni}_3\text{S}_2/\text{NF} // \text{Ti}_3\text{C}_2\text{T}_x$ ASC were tested in a two-electrode system. CV measurements of the $\text{Ni}_3\text{S}_2/\text{NF} // \text{Ti}_3\text{C}_2\text{T}_x$ device were performed at various scan rates (5–50 mV), as shown in Figure 9a. The CV curves revealed features of Faradaic behavior, and the device's shape was retained during the oxidation and reduction processes with an increasing scan rate. The charge/discharge curves of the device at various current densities are shown in Figure 9b, and they indicate that the device has excellent reversibility and high Coulombic efficiency.

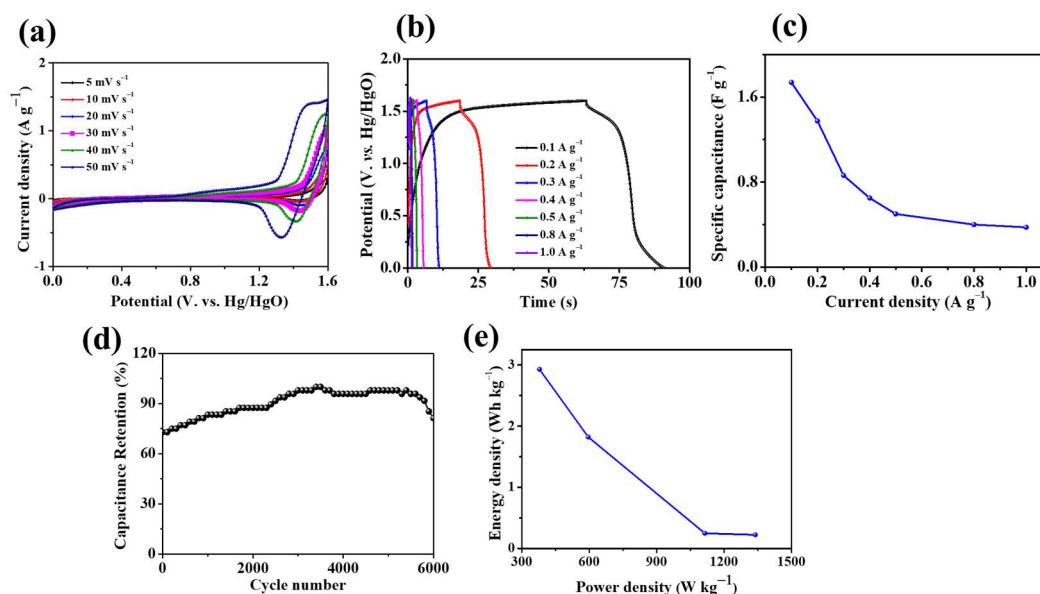


Figure 9. (a) CV curves, (b) GCD curves, (c) specific capacitance, (d) cycling performance (at 0.2 A g^{-1}), and (e) the Ragone plot of the $\text{Ni}_3\text{S}_2/\text{NF} // \text{Ti}_3\text{C}_2\text{T}_x$ ACS device.

The variation in the specific capacitance of the ASC device with the specific current is illustrated in Figure 9c. The specific capacitance decreased regularly with increasing

specific current. As shown in Figure 9d, during the first 3500 cycles, the capacitance retention of the $\text{Ni}_3\text{S}_2/\text{NF}/\text{Ti}_3\text{C}_2\text{T}_x$ increased steadily; this increase may be attributed to the activation process. The capacitance remained stable for the next 2000 cycles and then steadily dropped to 81.25% for the last 500 cycles, thereby demonstrating excellent cycling stability. Interestingly, the SC value of the ASC device initially increased, possibly because the proper wetting of the electrode active materials by KOH electrolyte improved the electrolyte/electrode contact [42]. These results show the superior capability of the $\text{Ni}_3\text{S}_2/\text{NF}/\text{Ti}_3\text{C}_2\text{T}_x$ ASC device with excellent stability and high performance during the long cycle life.

Figure 9e shows that the $\text{Ni}_3\text{S}_2/\text{NF}/\text{Ti}_3\text{C}_2\text{T}_x$ ASC device achieved an energy density of 2.93 Wh kg^{-1} with a power density of 379.16 W kg^{-1} . When the power density increased to $1338.83 \text{ W kg}^{-1}$, the energy density dropped to 0.22 Wh kg^{-1} . The energy density of our device exceeded that of the SCs reported by Xu et al. [43] and Ren et al. [44]; in these previous works, the SCs were based on carbon nanotubes (CNTs)- MnO_2 fibers ($17.26 \text{ nWh cm}^{-1}$ with the corresponding power density changing from $61.55 \mu\text{W cm}^{-1}$) and CNT-OMC fibers ($1.26 \times 10^{-6} \text{ nWh cm}^{-2}$ with the corresponding power density changing from 0.043 mW cm^{-2}), respectively. A symmetrical linear SC was assembled by Zhang et al. [45], and it consisted of a CNT- MnO_2 fiber electrode and a polyvinyl alcohol/ H_3PO_4 electrolyte and had an energy density of 86 nWh cm^{-1} . Table 1 lists the electrochemical performances of various electrode materials for comparison. The excellent electrochemical properties of the $\text{Ni}_3\text{S}_2/\text{NF}$ electrode are attributed to its unique structure, with many voids and abundant active sites for electrochemical reaction processes. This 3D porous honeycomb-like structure helps avoid congestion of electrolyte ions and increases the exposed surface area, thereby ensuring efficient ion diffusion and sufficient Faradaic redox reaction.

Table 1. Comparison of the electrochemical performances of the various electrode materials.

| Electrode Material | Electrolyte | Capacitance (Cs/Scan Rate) | Refs. |
|--|-------------|---|-----------|
| $\text{NiMoO}_4/\text{NiWO}_4$ | 3 M KOH | $1290 \text{ F g}^{-1}/2 \text{ A g}^{-1}$ | [46] |
| $\text{Co}_9\text{S}_8/\text{Ni}(\text{OH})_2$ | 2 M KOH | $1620 \text{ F g}^{-1}/0.5 \text{ A g}^{-1}$ | [47] |
| NiS/NiSe_2 | 2 M KOH | $1412 \text{ F g}^{-1}/0.5 \text{ A g}^{-1}$ | [48] |
| $\text{Ni}_3\text{S}_2/\text{Co}_9\text{S}_8$ | 2 M KOH | $925 \text{ F g}^{-1}/0.5 \text{ A g}^{-1}$ | [48] |
| $\text{Ni}_3\text{S}_4/\text{rGO}$ | 2 M KOH | $1830 \text{ F g}^{-1}/2 \text{ A g}^{-1}$ | [49] |
| $\text{Co-Ni}_3\text{S}_2$ | 2 M KOH | $1075.5 \text{ F g}^{-1}/1 \text{ A g}^{-1}$ | [50] |
| $\text{Ni}_3\text{S}_2/\text{NF}$ | 1 M KOH | $736.64 \text{ F g}^{-1}/0.8 \text{ A g}^{-1}$ | [51] |
| $\text{NiS}_2/\text{Ti}_3\text{C}_2\text{T}_x$ | 1 M KOH | $72.0 \text{ mAh g}^{-1}/1 \text{ A g}^{-1}$ | [52] |
| $\text{Ni}_3\text{S}_2/\text{Ni}$ | 6 M KOH | $945.71 \text{ F g}^{-1}/17.15 \text{ A g}^{-1}$ | [35] |
| $\text{Ni}_3\text{S}_2/\text{NF}$ | 1 M KOH | 1839.6 F g^{-1} (Corresponding specific capacity: $255.5 \text{ mAh g}^{-1}/3 \text{ A g}^{-1}$) | This work |

3. Materials and Methods

3.1. Preparation of the Nickel Sulphide Electrode

Sodium sulfides were supplied by Sigma Aldrich (St. Louis, MO, USA). NF (110 PPI pore density and a mass density of 320 g m^{-2}) were obtained from Artenano Company Limited (Hong Kong). Deionized water (DI) obtained from Millipore was used as a solvent in all experiments. Before use, the NF was prepared for experiment through previously reported routes. Ni foam of area $1 \times 1 \text{ cm}$ was thoroughly cleaned before the experiment by the following steps: It was degreased by immersion in acetone for 30 min; etched with dilute HCl (3.0 mol L^{-1}) for 15 min, and rinsed with DI water before drying. The precursor of $\text{Ni}(\text{OH})_2$ was described in our previous report [53]. First, 100 mmol of $\text{Ni}(\text{NO}_3)_2 \cdot 6\text{H}_2\text{O}$ and 25 mmol of hexamethylenetetramine were dissolved in 50 mL DI water, and cleaned NFs ($2 \times 4 \text{ cm}$) were placed in an autoclave at temperatures below $90 \text{ }^\circ\text{C}$ for 4 h. Subsequently, the as-obtained $\text{Ni}(\text{OH})_2/\text{NF}$ substrates were immersed in a 50 mL autoclave with 50 mmol Na_2S ; the autoclave was then heated to $120 \text{ }^\circ\text{C}$ and maintained at this temperature for 4 h to generate Ni_3S_2 . After the autoclave was allowed to cool to room temperature ($25 \text{ }^\circ\text{C}$), the

Ni₃S₂ was taken out of the autoclave and rinsed separately several times with anhydrous ethanol and distilled water.

3.2. Electrode Production

A previously published method [54] was used to clean NF. NiO/NF (1 × 1 cm) and Ni₃S₂/NF (1 × 1 cm) were coated with the treated NF. The Ti₃C₂T_x MXene composite, carbon black, and polytetrafluoroethylene (PTFE) solution (60 wt%) binder were mixed in a mass ratio of 8:1:1 to fabricate the working electrode. The homogeneous slurry was coated on the cleaned NF and dried for 12 h at 60 °C in a vacuum oven.

3.3. Fabrication of the ASC Device

The Ni₃S₂/NF//Ti₃C₂T_x MXene ASC device had a mass ratio of 1:6, and its positive and negative electrodes were Ni₃S₂/NF and Ti₃C₂T_x MXene, respectively. From the galvanostatic charge–discharge (GCD) curves, the specific capacitance of ASC (C_d) was calculated as follows [55]:

$$C_d = \frac{I \Delta t}{M \Delta V} \quad (10)$$

where I (A), Δt (s), M (g), and ΔV (V) are the applied discharge current, the discharge time, the total mass of the active material, and the potential window, respectively. The energy density (Wh kg^{−1}) and the power density (W kg^{−1}) of the ASC device were calculated from the GCD curve using the following equations [52]:

$$E = \frac{\int I \cdot V(t) dt}{3.6M} \quad (11)$$

$$P = 3600E / \Delta t, \quad (12)$$

where E (Wh kg^{−1}), I (A), $V(t)$ (V), P (W kg^{−1}), M (g), and Δt (s) are the energy density, the applied current, the potential window, the power density, the total mass of the active material, and the discharge time of the ASC device, respectively.

3.4. Electrochemical Measurements

The X-ray diffraction patterns were collected by an X-ray diffractometer (Rigaku, SmartLab, Tokyo, Japan). Cu K α X-ray radiation at 40 kV and 40 mA was used to identify the crystal structure and the phase purity of in situ grown Ni₃S₂ and NiO. Field-emission scanning electron microscopy (FE-SEM; Merlin Compact, Carl Zeiss NTS GmbH, Oberkochen, Germany), equipped with an instrument for energy dispersive X-ray spectroscopy (EDS), was performed at 15 kV to investigate the surface morphology and the elemental composition of individual nickel halides. Transmission electron microscopy (TEM) and selected-area electron diffraction patterns were operated on an FEI TalosF200x transmission electron microscope at 200 kV to further study the microstructure of the samples. To examine the surface area and pore-size distribution, the Brunauer–Emmett–Teller (BET) and Barrett–Joyner–Halenda (BJH) measurements were conducted using a Micrometrics ASAP2010 analyzer in N₂ gas under suitable humidity conditions. Electrochemical measurements of Ni₃S₂ and NiO electrode materials were conducted using an electrochemical workstation (Ivium vertex, Eindhoven, The Netherlands) based on cyclic voltammogram (CV) and GCD measurements. CV measurements were performed in the range of 0–0.8 V at different scan rates. The GCD scans of the Ni₃S₂ and NiO were obtained at various current rates within the potential window of 0–0.6 V in a 1 M KOH aqueous electrolyte solution. Hg/HgO and a platinum foil were used as the reference and counter electrode, respectively. The as-fabricated Ni₃S₂//MXene ASC device was assembled and tested in 1 M KOH electrolyte solution comprising a two-electrode system with a separator to avoid short circuiting.

4. Conclusions

In summary, a highly hierarchical 3D porous Ni₃S₂ nanosheet array was directly grown on NF via a hydrothermal method. This low-cost and simple-synthesis method can be extended to the commercial fabrication of the hybrid material for practical applications. Moreover, the pores among Ni₃S₂ NW facilitate electrolyte diffusion and electron transmission. Therefore, the Ni₃S₂/NF hybrid meets the requirements of rapid ion diffusion and transportation and shows high specific capacity, excellent rate performance, and good cycling stability; these properties are attributed to the 3D porous structure, the enhanced conductivity, and the facile electrolyte penetration of Ni₃S₂ NW. Furthermore, the synthesized Ni₃S₂ NW possessed high specific capacitance and excellent stability during electrochemical analysis. Hence, this material may be promising for electrodes in SC applications. The unique architecture of the Ni₃S₂ electrode provides excellent electrochemical performance with small charge transfer resistance, which endows the as-prepared Ni₃S₂ electrode with high capacitance as well as excellent cycling stability. The above self-growth of the Ni₃S₂ electrode makes it appealing for other applications, such as catalysts and sensor batteries. Furthermore, the hydrothermal fabrication method is simple and cost-effective, and the fabricated material is binder-free. This approach can be adopted in the fabrication of other self-supported metal oxide electrodes for SCs or energy storage applications.

Author Contributions: Conceptualization, Q.X. and L.S.; methodology, formal analysis, investigation, original draft preparation, C.S. and G.F.; data curation, conceptualization, writing—review and editing, N.M.S., A.Z. and J.D.; writing—review and editing, visualization, funding acquisition, supervision, Q.X., L.S., K.L., A.Z., C.S., N.M.S., G.F. and J.D. All authors have read and agreed to the published version of the manuscript.

Funding: We appreciate support from the National Natural Science Foundation of China (51772077), the China Postdoctoral Science Foundation (2019M652537), the Henan Postdoctoral Foundation (19030065), the Henan Province Key Science and Technology Research Projects (202102310628), the Foundation of Henan Educational Committee (20B430006), and the Doctoral Fund Project of Henan Polytechnic University (B2019-41).

Conflicts of Interest: The authors declare no conflict of interest.

Sample Availability: Not applicable.

References

1. Simon, P.; Gogotsi, Y. Materials for electrochemical capacitors. *Nat. Mater.* **2008**, *7*, 845–854. [[CrossRef](#)] [[PubMed](#)]
2. Yan, J.; Wang, Q.; Wei, T.; Fan, Z.J. Recent Advances in Design and Fabrication of Electrochemical Supercapacitors with High Energy Densities. *Adv. Energy Mater.* **2014**, *4*, 1300816. [[CrossRef](#)]
3. Liu, F.; Su, H.; Jin, L.; Zhang, H.; Chu, X.; Yang, W. Facile synthesis of ultrafine cobalt oxide nanoparticles for high-performance supercapacitors. *J. Colloid. Interface Sci.* **2017**, *505*, 796–804. [[CrossRef](#)] [[PubMed](#)]
4. Liu, F.; Gao, Y.; Zhang, C.; Huang, H.; Yan, C.; Chu, X.; Xu, Z.; Wang, Z.; Zhang, H.; Xiao, X.; et al. Highly microporous carbon with nitrogen-doping derived from natural biowaste for high-performance flexible solid-state supercapacitor. *J. Colloid. Interface Sci.* **2019**, *548*, 322–332. [[CrossRef](#)] [[PubMed](#)]
5. Su, H.; Zhang, H.; Liu, F.; Chun, F.; Zhang, B.; Chu, X.; Huang, H.; Deng, W.; Gu, B.; Zhang, H.; et al. High power supercapacitors based on hierarchically porous sheet-like nanocarbons with ionic liquid electrolytes. *Chem. Eng. J.* **2017**, *322*, 73–81. [[CrossRef](#)]
6. Rakhi, R.; Chen, W.; Hedhili, M.N.; Cha, D.; Alshareef, H.N. Enhanced rate performance of mesoporous Co₃O₄ nanosheet supercapacitor electrodes by hydrous RuO₂ nanoparticle decoration. *ACS Appl. Mater. Interfaces* **2014**, *6*, 4196–4206. [[CrossRef](#)]
7. Xia, Q.X.; Yun, J.M.; Mane, R.S.; Li, L.; Fu, J.; Lim, J.H.; Kim, K.H. Enhanced electrochemical activity of perforated graphene in nickel-oxide-based supercapacitors and fabrication of potential asymmetric supercapacitors. *Sustain. Energy Fuels* **2017**, *1*, 529–539. [[CrossRef](#)]
8. He, Y.; Chen, W.; Li, X.; Zhang, Z.; Fu, J.; Zhao, C.; Xie, E. Freestanding three-dimensional graphene/MnO₂ composite networks as ultralight and flexible supercapacitor electrodes. *ACS Nano* **2012**, *7*, 174–182. [[CrossRef](#)]
9. Hui, K.N.; San Hui, K.; Tang, Z.; Jadhav, V.; Xia, Q.X. Hierarchical chestnut-like MnCo₂O₄ nanoneedles grown on nickel foam as binder-free electrode for high energy density asymmetric supercapacitors. *J. Power Sources* **2016**, *330*, 195–203. [[CrossRef](#)]
10. Xie, M.; Xu, Z.; Duan, S.; Tian, Z.; Zhang, Y.; Xiang, K.; Lin, M.; Guo, X.; Ding, W. Facile growth of homogeneous Ni(OH)₂ coating on carbon nanosheets for high-performance asymmetric supercapacitor applications. *Nano Res.* **2017**, *11*, 216–224. [[CrossRef](#)]

11. Xie, M.; Duan, S.; Shen, Y.; Fang, K.; Wang, Y.; Lin, M.; Guo, X. In-Situ-Grown Mg(OH)₂-Derived Hybrid α -Ni(OH)₂ for Highly Stable Supercapacitor. *ACS Energy Lett.* **2016**, *1*, 814–819. [[CrossRef](#)]
12. Wang, X.; Song, H.; Ma, S.; Li, M.; He, G.; Xie, M.; Guo, X. Template ion-exchange synthesis of Co-Ni composite hydroxides nanosheets for supercapacitor with unprecedented rate capability. *Chem. Eng. J.* **2022**, *432*, 134319. [[CrossRef](#)]
13. Scrosati, B.; Garche, J. Lithium batteries: Status, prospects and future. *J. Power Sources* **2010**, *195*, 2419–2430. [[CrossRef](#)]
14. Li, Y.; Huang, B.; Zhao, X.; Luo, Z.; Liang, S.; Qin, H.; Chen, L. Zeolitic imidazolate framework-L-assisted synthesis of inorganic and organic anion-intercalated hetero-trimetallic layered double hydroxide sheets as advanced electrode materials for aqueous asymmetric super-capacitor battery. *J. Power Sources* **2022**, *527*, 231149. [[CrossRef](#)]
15. Li, Y.; Luo, Z.; Qin, H.; Liang, S.; Chen, L.; Wang, H.; Zhao, C.; Chen, S. Benzoate anions-intercalated cobalt-nickel layered hydroxide nanobelts as high-performance electrode materials for aqueous hybrid supercapacitors. *J. Colloid. Interface Sci.* **2021**, *582 Pt B*, 842–851. [[CrossRef](#)]
16. Zhao, C.; Zhu, J.; Jiang, Y.; Gao, F.; Xie, L.; Chen, L. Facile synthesis of spinel MgCo₂O₄ nanosheets for high-performance asymmetric supercapacitors. *Mater. Lett.* **2020**, *271*, 127799. [[CrossRef](#)]
17. Zhao, C.; Liang, S.; Jiang, Y.; Gao, F.; Xie, L.; Chen, L. Mn doped Co(OH)₂ nanosheets as electrode materials for high performance supercapacitors. *Mater. Lett.* **2020**, *270*, 127751. [[CrossRef](#)]
18. Li, Y.; Luo, Z.; Liang, S.; Qin, H.; Zhao, X.; Chen, L.; Wang, H.; Chen, S. Two-dimensional porous zinc cobalt sulfide nanosheet arrays with superior electrochemical performance for supercapatteries. *J. Mater. Sci. Technol.* **2021**, *89*, 199–208. [[CrossRef](#)]
19. Liang, J.-Y.; Zeng, X.-X.; Zhang, X.-D.; Wang, P.-F.; Ma, J.-Y.; Yin, Y.-X.; Wu, X.-W.; Guo, Y.-G.; Wan, L.-J. Mitigating Interfacial Potential Drop of Cathode–Solid Electrolyte via Ionic Conductor Layer To Enhance Interface Dynamics for Solid Batteries. *J. Am. Chem. Soc.* **2018**, *140*, 6767–6770. [[CrossRef](#)]
20. Li, X.-X.; Chen, G.-F.; Xiao, K.; Li, N.; Ma, T.-Y.; Liu, Z.-Q. Self-Supported Amorphous-Edge Nickel Sulfide Nanobrush for Excellent Energy Storage. *Electrochim. Acta* **2017**, *255*, 153–159. [[CrossRef](#)]
21. Cai, H.; Li, X.; Li, G.; Xia, H.; Wang, P.; Sun, P.; Huang, J.; Wang, L.; Yang, Y. Synthesis of honeycomb-like nickel-manganese sulfide composite nanosheets as advanced battery-type electrodes for hybrid supercapacitor. *Mater. Lett.* **2019**, *255*, 126505. [[CrossRef](#)]
22. Wei, C.; Cheng, C.; Zhao, J.; Wang, Y.; Cheng, Y.; Xu, Y.; Du, W.; Pang, H. NiS Hollow Spheres for High-Performance Supercapacitors and Non-Enzymatic Glucose Sensors. *Chem.–Asian J.* **2015**, *10*, 679–686. [[CrossRef](#)]
23. Wang, N.; Pan, Q.; Yang, X.; Zhu, H.; Ding, G.; Jia, Z.; Wu, Y.; Zhao, L. High Performance Asymmetric Supercapacitor Based on Ni₃S₂/MoS₂ Nanoparticles. *ACS Appl. Nano Mater.* **2019**, *2*, 4910–4920. [[CrossRef](#)]
24. Wang, L.; Liu, J.; Zhang, L.L.; Dai, B.; Xu, M.; Ji, M.; Zhao, X.S.; Cao, C.; Zhang, J.; Zhu, H. Rigid three-dimensional Ni₃S₄ nanosheet frames: Controlled synthesis and their enhanced electrochemical performance. *RSC Adv.* **2015**, *5*, 8422–8426. [[CrossRef](#)]
25. Mu, X.; Wang, D.; Du, F.; Chen, G.; Wang, C.; Wei, Y.; Gogotsi, Y.; Gao, Y.; Dall’Agnese, Y. Revealing the Pseudo-Intercalation Charge Storage Mechanism of MXenes in Acidic Electrolyte. *Adv. Funct. Mater.* **2019**, *29*, 1902953. [[CrossRef](#)]
26. Ando, Y.; Okubo, M.; Yamada, A.; Otani, M. Capacitive versus Pseudocapacitive Storage in MXene. *Adv. Funct. Mater.* **2020**, *30*, 2000820. [[CrossRef](#)]
27. Chen, C.; Pang, D.; Wang, X.; Chen, G.; Du, F.; Gao, Y. Electrochemical Behavior of Vanadium Carbide in Neutral Aqueous Electrolytes. *Chin. Phys. Lett.* **2021**, *38*, 058201. [[CrossRef](#)]
28. Xiao, N.; Lu, X.-H.; Yan, W.-J.; Wen, M.-X.; Sun, W.; Xu, J.-L.; Sun, Y.-H.; Sun, Q. Self-template synthesis of hollow nano-spherical nickel silicate/nickel sulfide composite and its application for lithium-sulfur battery. *Mater. Lett.* **2021**, *300*, 130215. [[CrossRef](#)]
29. Shen, M.; Liu, J.; Liu, T.; Yang, C.; He, Y.; Li, Z.; Li, J.; Qian, D. Oxidant-assisted direct-sulfidization of nickel foam toward a self-supported hierarchical Ni₃S₂@Ni electrode for asymmetric all-solid-state supercapacitors. *J. Power Sources* **2020**, *448*, 227408. [[CrossRef](#)]
30. Du, X.; Ma, G.; Zhang, X. Cobalt and nitrogen co-doped Ni₃S₂ nanoflowers on nickel foam as high-efficiency electrocatalysts for overall water splitting in alkaline media. *Dalton Trans.* **2021**, *50*, 8955–8962. [[CrossRef](#)]
31. Zhao, C.; Zhang, Z.; Wang, Q.; Min, S.; Qian, X. Vertically oriented Ni₃S₂/RGO/Ni₃S₂ nanosheets on Ni foam for superior supercapacitors. *RSC Adv.* **2015**, *5*, 63528–63536. [[CrossRef](#)]
32. Moradabadi, A.; Kaghazchi, P. Mechanism of Li intercalation/deintercalation into/from the surface of LiCoO₂. *Phys. Chem. Chem. Phys.* **2015**, *17*, 22917–22922. [[CrossRef](#)] [[PubMed](#)]
33. Pfaffmann, L.; Birkenmaier, C.; Müller, M.; Bauer, W.; Mitsch, T.; Feinauer, J.; Krämer, Y.; Scheiba, F.; Hintennach, A.; Schleid, T.; et al. Investigation of the electrochemically active surface area and lithium diffusion in graphite anodes by a novel OsO₄ staining method. *J. Power Sources* **2016**, *307*, 762–771. [[CrossRef](#)]
34. Luo, X.-y.; Chen, Y.; Mo, Y. A review of charge storage in porous carbon-based supercapacitors. *New Carbon Mater.* **2021**, *36*, 49–68. [[CrossRef](#)]
35. Chen, S.; Li, Y.; Wu, B.; Wu, Z.; Li, F.; Wu, J.; Liu, P.; Li, H. 3D meso/macroporous Ni₃S₂@Ni composite electrode for high-performance supercapacitor. *Electrochim. Acta* **2018**, *275*, 40–49. [[CrossRef](#)]
36. Wang, X.; Gao, J.; Wu, X.; Wang, X.; Que, R.; Wu, K. A facile one-pot hydrothermal synthesis of Co₉S₈/Ni₃S₂ nanoflakes for supercapacitor application. *RSC Adv.* **2016**, *6*, 54142–54148. [[CrossRef](#)]
37. Nandhini, S.; Muralidharan, G. Graphene encapsulated NiS/Ni₃S₄ mesoporous nanostructure: A superlative high energy supercapacitor device with excellent cycling performance. *Electrochim. Acta* **2021**, *365*, 137367. [[CrossRef](#)]

38. Pu, X.; Zhao, D.; Fu, C.; Chen, Z.; Cao, S.; Wang, C.; Cao, Y. Understanding and Calibration of Charge Storage Mechanism in Cyclic Voltammetry Curves. *Angew. Chem. Int. Ed.* **2021**, *60*, 21310–21318. [[CrossRef](#)]
39. Kudchi, R.S.; Shetti, N.P.; Malode, S.J.; Todakar, A.B. Electroanalysis of an antihistamine drug at nano structured modified electrode. *Mater. Today Proc.* **2019**, *18*, 558–565. [[CrossRef](#)]
40. Zhao, Y.; Guo, J.; Liu, A.; Ma, T. 2D heterostructure comprised of Ni₃S₂/d-Ti₃C₂ supported on Ni foam as binder-free electrode for hybrid supercapacitor. *J. Alloys Compd.* **2020**, *814*, 152271. [[CrossRef](#)]
41. Xia, Q.X.; Fu, J.; Yun, J.M.; Mane, R.S.; Kim, K.H. High volumetric energy density annealed-MXene-nickel oxide/MXene asymmetric supercapacitor. *RSC Adv.* **2017**, *7*, 11000–11011. [[CrossRef](#)]
42. Ghosh, S.; Sharath Kumar, J.; Chandra Murmu, N.; Sankar Ganesh, R.; Inokawa, H.; Kuila, T. Development of carbon coated NiS₂ as positive electrode material for high performance asymmetric supercapacitor. *Compos. Part B Eng.* **2019**, *177*, 107373. [[CrossRef](#)]
43. Xu, P.; Wei, B.; Cao, Z.; Zheng, J.; Gong, K.; Li, F.; Yu, J.; Li, Q.; Lu, W.; Byun, J.-H.; et al. Stretchable Wire-Shaped Asymmetric Supercapacitors Based on Pristine and MnO₂ Coated Carbon Nanotube Fibers. *ACS Nano* **2015**, *9*, 6088–6096. [[CrossRef](#)] [[PubMed](#)]
44. Ren, J.; Bai, W.; Guan, G.; Zhang, Y.; Peng, H. Flexible and weaveable capacitor wire based on a carbon nanocomposite fiber. *Adv. Mater.* **2013**, *25*, 5965–5970. [[CrossRef](#)]
45. Zhang, L.; Zhang, X.; Wang, J.; Seveno, D.; Fransaeer, J.; Locquet, J.P.; Seo, J.W. Carbon Nanotube Fibers Decorated with MnO₂ for Wire-Shaped Supercapacitor. *Molecules* **2021**, *26*, 3479. [[CrossRef](#)]
46. Reddy, A.E.; Anitha, T.; Muralee Gopi, C.V.V.; Srinivasa Rao, S.; Kim, H.J. NiMoO₄@NiWO₄ honeycombs as a high performance electrode material for supercapacitor applications. *Dalton Trans.* **2018**, *47*, 9057–9063. [[CrossRef](#)]
47. Wen, J.; Li, S.; Li, B.; Song, Z.; Wang, H.; Xiong, R.; Fang, G. Synthesis of three dimensional Co₉S₈ nanorod@Ni(OH)₂ nanosheet core-shell structure for high performance supercapacitor application. *J. Power Sources* **2015**, *284*, 279–286. [[CrossRef](#)]
48. Wei, W.; Mi, L.; Gao, Y.; Zheng, Z.; Chen, W.; Guan, X. Partial Ion-Exchange of Nickel-Sulfide-Derived Electrodes for High Performance Supercapacitors. *Chem. Mater.* **2014**, *26*, 3418–3426. [[CrossRef](#)]
49. Hu, Q.; Zou, X.; Huang, Y.; Wei, Y.; Wang, Y.; Chen, F.; Xiang, B.; Wu, Q.; Li, W. Graphene oxide-drove transformation of NiS/Ni₃S₄ microbars towards Ni₃S₄ polyhedrons for supercapacitor. *J. Colloid. Interface Sci.* **2020**, *559*, 115–123. [[CrossRef](#)]
50. Chang, Y.; Sui, Y.; Qi, J.; Jiang, L.; He, Y.; Wei, F.; Meng, Q.; Jin, Y. Facile synthesis of Ni₃S₂ and Co₉S₈ double-size nanoparticles decorated on rGO for high-performance supercapacitor electrode materials. *Electrochim. Acta* **2017**, *226*, 69–78. [[CrossRef](#)]
51. Chen, L.; Guan, L.; Tao, J. Morphology control of Ni₃S₂ multiple structures and their effect on supercapacitor performances. *J. Mater. Sci.* **2019**, *54*, 12737–12746. [[CrossRef](#)]
52. Si, L.; Xia, Q.; Liu, K.; Guo, W.; Shinde, N.; Wang, L.; Hu, Q.; Zhou, A. Hydrothermal synthesis of layered NiS₂/Ti₃C₂Tx composite electrode for supercapacitors. *Mater. Chem. Phys.* **2022**, *291*, 126733. [[CrossRef](#)]
53. Xia, Q.; Hui, K.S.; Hui, K.; Hwang, D.; Lee, S.; Zhou, W.; Cho, Y.; Kwon, S.; Wang, Q.; Son, Y. A facile synthesis method of hierarchically porous NiO nanosheets. *Mater. Lett.* **2012**, *69*, 69–71. [[CrossRef](#)]
54. Xia, Q.X.; San Hui, K.; Hui, K.N.; Kim, S.D.; Lim, J.H.; Choi, S.Y.; Zhang, L.J.; Mane, R.S.; Yun, J.M.; Kim, K.H. Facile synthesis of manganese carbonate quantum dots/Ni(HCO₃)₂-MnCO₃ composites as advanced cathode materials for high energy density asymmetric supercapacitors. *J. Mater. Chem. A* **2015**, *3*, 22102–22117. [[CrossRef](#)]
55. Liu, K.; Xia, Q.; Si, L.; Kong, Y.; Shinde, N.; Wang, L.; Wang, J.; Hu, Q.; Zhou, A. Defect engineered Ti₃C₂Tx MXene electrodes by phosphorus doping with enhanced kinetics for supercapacitors. *Electrochim. Acta* **2022**, *435*, 141372. [[CrossRef](#)]

Disclaimer/Publisher’s Note: The statements, opinions and data contained in all publications are solely those of the individual author(s) and contributor(s) and not of MDPI and/or the editor(s). MDPI and/or the editor(s) disclaim responsibility for any injury to people or property resulting from any ideas, methods, instructions or products referred to in the content.